RESEARCH ARTICLE

Editor's Choice

ADVANCED
MATERIALS
INTERFACES

www.advmatinterfaces.de

Combinatorial Vacuum-Deposition of Wide Bandgap Perovskite Films and Solar Cells

Isidora Susic, Adi Kama, Lidón Gil-Escrig,* Chris Dreessen, Francisco Palazon, David Cahen, Michele Sessolo,* and Henk J. Bolink

The development of vacuum-deposited perovskite materials and devices is partially slowed down by the minor research effort in this direction, due to the high cost of the required research tools. But there is also another factor, thermal co-deposition in high vacuum involves the simultaneous sublimation of several precursors with an overall deposition rate in the range of few Å s^{-1}. This leads to a deposition time of hours with only a single set of process parameters per batch, hence to a long timeframe to optimize even a single perovskite composition. Here we report the combinatorial vacuum deposition of wide bandgap perovskites using 4 sources and a non-rotating sample holder. By using small pixel substrates, more than 100 solar cells can be produced with different perovskite absorbers in a single deposition run. The materials are characterized by spatially resolved methods, including optical, morphological, and structural techniques. By fine-tuning of the deposition rates, the gradient can be altered and the best-performing formulations in standard depositions with rotation can be reproduced. This is viewed as an approach that can serve as a basis to prototype other compositions, overcoming the current limitations of vacuum deposition as a research tool for perovskite films.

1. Introduction

The rapid advancement of hybrid halide perovskites, ABX$_3$, where *A* is a monovalent cation, *B* is a group IV divalent cation, and *X* is a halide, and their unique optoelectronic features make them a viable alternative as absorber materials to traditional PV systems.[1] The current record power conversion efficiency (PCE) for a single junction halide perovskite solar cell is above 25%, which is achieved with B = Pb^{2+}.[2] The beneficial optoelectronic features, such as sharp and efficient optical absorption,[3] long diffusion length,[4,5] and low optically and electrically active defect concentrations,[6–9] are credited with the achievement of efficient optoelectronic devices. One of the key benefits of using halide perovskites is the ease with which high-quality semiconducting films are made using simple solution-based small-scale methods like spin-coating, but also scalable ones such as slot-die coating.[10]

Besides solution-based deposition, high-efficiency perovskite solar cells are increasingly being reported also using physical vapor deposition techniques.[11–15] Vapor deposition processes offer several advantages over solution-based methods, including no dependence on (toxic) solvents and solubility of the precursors, precise control over film thickness,[16,17] and the straightforward fabrication of multilayer architectures. Importantly, thermal vacuum deposition is widely used in the semiconductor industry and can be scaled up to large substrates,[18] moving closer to the commercialization of perovskite solar cells.

The structural stability of perovskites can be estimated using a relation between the known (average) ionic radii of the ions that make up the material, which yields the Goldschmidt tolerance factor.[19] *A*-site cations such as Cs$^+$, methylammonium (MA$^+$), and formamidinium (FA$^+$), have different atomic radii, which affect the perovskite structure distinctly.[20,21] To minimize perovskite toxicity, the lead on the *B* site can be substituted with tin (Sn^{2+}) or germanium (Ge^{2+}).[22,23] Different halides (iodide, bromide, or chloride) or their combinations can be used for bandgap tuning and to improve stability.[24,25] Using only nine ions, thousands of distinct perovskite compositions can be fabricated to gain improved properties, efficiency, or stability.

I. Susic, L. Gil-Escrig, C. Dreessen, M. Sessolo, H. J. Bolink
Instituto de Ciencia Molecular
Universidad de Valencia
C/Catedrático J. Beltrán 2, Paterna 46980, Spain
E-mail: lidon.gil@uv.es; michele.sessolo@uv.es

A. Kama, D. Cahen
Department of Chemistry and Bar-Ilan Institute for Nanotechnology & Advanced Materials
Bar-Ilan University
Ramat Gan 5290002, Israel

F. Palazon
Departamento de Ingeniería Química y Ambiental
Universidad Politécnica de Cartagena
Aulario II, Campus de Alfonso XIII, Cartagena 30203, Spain

D. Cahen
Department of Molecular Chemistry and Materials Science
Weizmann Institute of Science
Rehovot 7610001, Israel

The ORCID identification number(s) for the author(s) of this article can be found under https://doi.org/10.1002/admi.202202271.

Vacuum deposition becomes more challenging when targeting complex perovskite compositions. The simultaneous co-sublimation of perovskite precursors limits the complexity of the perovskite formulation, as the number of thermal sources limits the number of precursors that can be co-sublimed. Narrow bandgap perovskites such as formamidinium lead iodide ($FAPbI_3$) have been prepared and stabilized in vacuum processes involving 2 and up to 4 sources.[26–29] Similarly, wide bandgap hybrid perovskites have been prepared by co-sublimation using 2 and up to 4 thermal sources, with an increasing number of A-cations and halides. Vacuum-deposited $MAPb(I_{1-x}Br_x)_3$ films and solar cells have been prepared with 2- and 3-sources processes, where stable films can be obtained only with x up to 0.2 (1.7 eV).[30,31] For higher bromide contents, the perovskite demixes into iodide- and bromide-rich phases in a process known as "halide segregation",[32–34] which can be alleviated (for formulations containing <25% Br) by adding mixed A-site cations such as cesium and formamidinium (Cs^+ and FA^+).[32,35,36] Mixed-cation and mixed-halide perovskites of the type $FA_{1-n}Cs_nPb(I_{1-x}Br_x)_3$ have also been prepared via vacuum-deposition, either with 3-source,[37,38] or with 4 source-processes.[39,40] We have also shown the preparation of triple and quadruple cation perovskite films and solar cells,[41,42] which is possible if two precursors are evaporated from the same thermal source.[43,44] The development of vacuum-deposited perovskite materials and devices are partially slowed down by the minor research effort in this direction, at least when compared with the field of solution-processed perovskites. But there is also another factor, thermal co-deposition in high vacuum (e.g., 10^{-6} mbar) involves the simultaneous sublimation of several precursors with an overall deposition rate in the range of 1–4 Å s^{-1}. This leads to a deposition time of >1 h (typically 2 h considering chamber evacuation and venting). Importantly, in typical deposition chambers, in one deposition run only a single set of parameters can be used (i.e., a set of deposition rates for a certain set of precursors). This leads to a longer timeframe for optimizing even a single perovskite composition.

Combinatorial materials science (CMS) is a method that can be used to accelerate the study of compositionally varying perovskites.[45] CMS is widely used in the research and development of catalysts, biomaterials, and nanomaterials.[46] When CMS is applied to thin films, a gradient with variation of deposition parameters such as composition, thickness, or temperature is deposited on a single large area substrate, referred to as a library, forming a set of experiments or materials in a single deposition run.[47–50] The library of materials is then investigated with spatially resolved high-throughput measurements, to pinpoint those with more interesting physical or chemical properties, which can be later replicated as isolated homogeneous materials. As described by Potyrailo et al., the terms "combinatorial materials screening" and "high-throughput experimentation" are typically interchangeably applied for all types of automated parallel and rapid sequential evaluation processes of materials and process parameters that include truly combinatorial permutations or their selected subsets.[51] CMS with high-throughput analysis of the products of the syntheses has also been applied to the development of halide perovskites. For example, the phase transition of the $CsPb(I_xBr_{1-x})_3$ perovskite was studied using inkjet printing by mixing two precursor solutions with different ratios to form a continuous compositional spread (CCS).[52] Another study concerned the degradation mechanism of the CCS of Br and I in $MAPb(I_xBr_{1-x})_3$ perovskite.[53] Deposition of the CCS using solution-based methods is limited as it depends on solvent polarity, pH, boiling point, and solubility. Solvents play essential roles in controlling not only the solubility but also the nucleation and growth of the perovskite film.[54] Therefore, systematic changes in composition/precursors also affect the coverage, thickness, and density of the perovskite films.[55] High throughput synthesis has also been used to develop perovskite nanocrystals in a droplet-based microfluidic platform, producing tens of compositions within minutes.[56] Robotic, high throughput synthesis has been applied to the preparation of low dimensional perovskite crystals,[57] as well as to perovskite films.[58] The latter was achieved via a combinatorial synthesis with high-throughput characterization with a high level of complexity and automation. Such platforms are extremely promising for the future development of advanced perovskite formulations and have already been applied to screen perovskite compositions with state-of-the-art stability in solar cells.[59] Simple perovskite CCS produced by vacuum co-evaporation has also been reported. Compositional gradients have been obtained using two thermal sources with a non-rotating substrate, resulting in linear CCS of two precursors. The compositional gradient formed during evaporation can be systematically reproduced in a controlled process. Simple binary compounds such as $MAPbI_3$,[60] $CsPbI_3$,[61,62] $CsPbBr_3$,[63] have been studied for application in solar cells and light-emitting diodes (LEDs). Yet, only linear compositional gradients of binary compounds have been reported to date.

Here we report the combinatorial vacuum deposition of wide bandgap perovskites of the type $FA_{1-n}Cs_nPb(I_{1-x}Br_x)_3$, by using 4 sources and a non-rotating sample holder. With an initial set of deposition rates for each precursor, calculated based on the target perovskite stoichiometry, we run a combinatorial deposition and high throughput characterization. By using small pixel substrates, we can produce >100 solar cells with different perovskite absorbers in a single deposition run. The materials are thoroughly characterized by spatially resolved and high throughput methods, including optical, morphological, and structural techniques. By subsequent fine-tuning of the deposition rates, we can alter the gradient and reproduce the best-performing formulations in standard depositions with rotation. We view this as an approach that can accelerate the discovery of materials, and serve as a basis to prototype other compositions (low bandgap and lead-free), overcoming the current limitations of vacuum deposition as a research tool for perovskite films.

2. Results and Discussion

The vacuum chamber used for this study is equipped with 4 deposition sources located 90° from each other, at a vertical distance of 25 cm from the substrate holder. Each thermal source is equipped with a quartz crystal microbalance (QCM) thickness sensor that monitors the sublimation rate, and a fifth sensor located in the proximity of the sample holder monitors the overall deposition rate. The substrate holder is fixed with
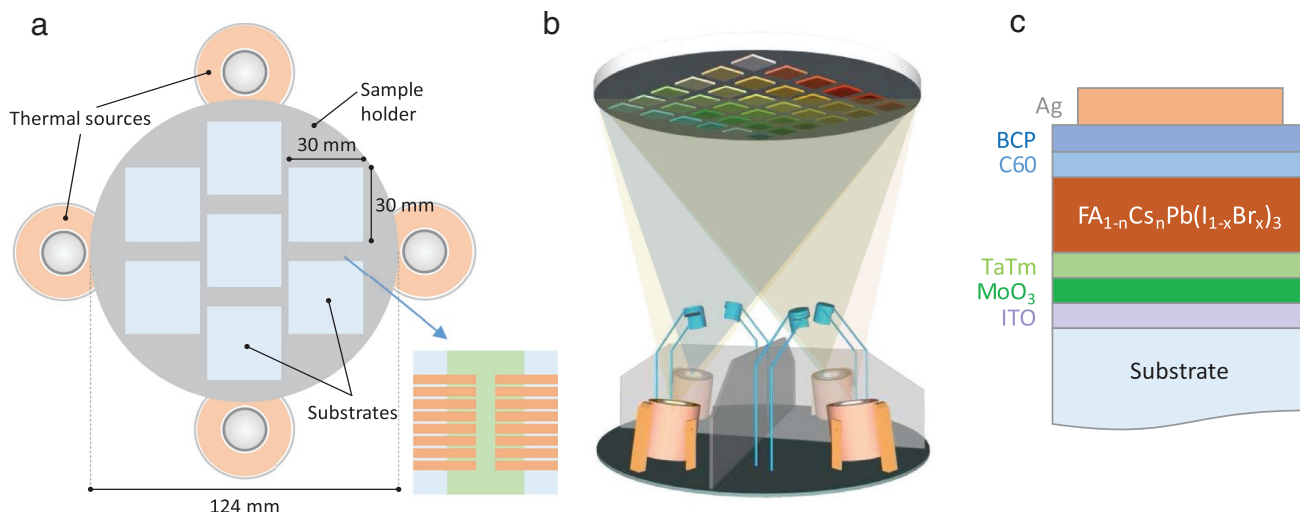
Figure 1. Details of the setup and device layout used in the combinatorial study. a) Top view of the substrate holder, position of the thermal sources, dimensions and layout of a single substrate. b) Without sample rotation, a gradient of each precursor is deposited on the substrate, resulting in CCS library of thin film perovskites. c) Device architecture that was used in this study.

respect to the sources (as depicted in **Figure 1**a) and can accommodate seven 30×30 mm square substrates to form a CCS of $FA_{1-n}Cs_nPb(I_{1-x}Br_x)_3$. To ensure enough spatial resolution, each substrate is patterned by lithography so that it can accommodate 16 solar cells (defined by the geometry of the top metal electrode using shadow masks, 8.25 mm²), resulting in 112 measurement points and working solar cells for a single deposition run.

We chose to study a well-known wide bandgap halide perovskite, targeting the approximate stoichiometry $FA_{0.6}Cs_{0.4}Pb(I_{0.8}Br_{0.2})_3$, and using FAI, CsI, PbI_2, and $PbBr_2$ as the precursors. The starting deposition rates (r) are chosen by fixing $r(PbI_2)$ at 1 Å s⁻¹. Using the PbI_2 density and molecular weight, we calculate the $r(PbI_2)$ in mol s⁻¹. Then, the deposition rates (in mol s⁻¹) of the other precursors (FAI, CsI, and $PbBr_2$) are calculated simply considering the target stoichiometry. Finally, the corresponding deposition rates in Å s⁻¹ are calculated considering the density and molecular weight of each precursor (**Table 1**). With this set of initial deposition rates, we run the vacuum deposition of perovskite films with a fixed sample holder, obtaining a CCS library because of the gradients formed by each of the 4 precursors (Figure 1b). The glass substrates contain patterned indium tin oxide (ITO), which are coated with MoO_3 (5 nm)/TaTm (10 nm) bilayers used as hole transport

layers (HTLs), with TaTm being $N4,N4,N4'',N4''$-tetra([1,1'-biphenyl]-4-yl)-[1,1':4',1''-terphenyl]-4,4''-diamine (TaTm). The combinatorial deposition of the perovskite is then carried out until a nominal thickness at the substrate sensor of 500 nm. Samples are finished with a 25 nm thick fullerene (C_{60}) film as an electron transport layer and 8 nm bathocuproine (BCP) as a buffer layer. One hundred nanometers thick Ag is deposited using a shadow mask to form 16 individual electrodes on each substrate (Figure 1c).

We initially analyzed the performance of the perovskite solar cells by measuring all the 112 pixels under simulated solar illumination. Each substrate containing 16 solar cells is measured with a customized automatic system, and the resulting PV parameters for the 7 substrates are depicted as color maps, with the position of each substrate on the holder with respect to the source location. In **Figure 2**, the color maps for the main PV indicators are reported, together with the current density versus voltage (J–V) curves under illumination for each substrate.

In Figure 2, a gradient of the short circuit current density (J_{sc}) is clearly visible, with lower photocurrent (≈8 mA cm⁻²) in pixels located in the vicinity of the $PbBr_2$ and PbI_2 sources, and higher J_{sc} (up to 17 mA cm⁻²) for those closer to the CsI and FAI sources. As discussed in more detail in the following, this is related to the higher Br content in the top part of the map, resulting in wider bandgap perovskites due to increased electronegativity when exchanging I with Br.[64] This hypothesis is also supported by the trend in open circuit voltage (V_{oc}), which is higher (reaching values up to 1.2 V) in the top-central part of the material library. We noticed a slightly lower V_{oc} for the devices near the $PbBr_2$ source, indicating that other loss mechanisms are present in Br-rich materials.[65,66] However, the V_{oc} does not vary substantially within the library, as the minimum values are still in the range of 1.16 V. The fill factor (FF) is more directly aligned with the gradient of CsI, as the highest value (≈80%) is found on the left side of the sample holder, where the CsI content is expected to be higher.

Table 1. Initial set of deposition rates of the perovskite precursors, calculated taking into account the target stoichiometry of the wide bandgap perovskite $FA_{0.6}Cs_{0.4}Pb(I_{0.8}Br_{0.2})_3$ (*$r(PbI_2)$ is fixed at 1.0 Å s⁻¹ as a starting point).

	Molar ratio	ρ [g cm⁻³]	MW [g mol⁻¹]	r [mol s⁻¹]	r [Å s⁻¹]
PbI_2	0.8	6.16	461.01	1.34×10^{-10}	1.0*
$PbBr_2$	0.2	6.66	367.01	3.35×10^{-11}	0.2
FAI	0.6	2.22	171.97	1.00×10^{-10}	0.8
CsI	0.4	4.44	259.81	6.78×10^{-11}	0.4

**ADVANCED
SCIENCE NEWS**
www.advancedsciencenews.com

**ADVANCED
MATERIALS
INTERFACES**
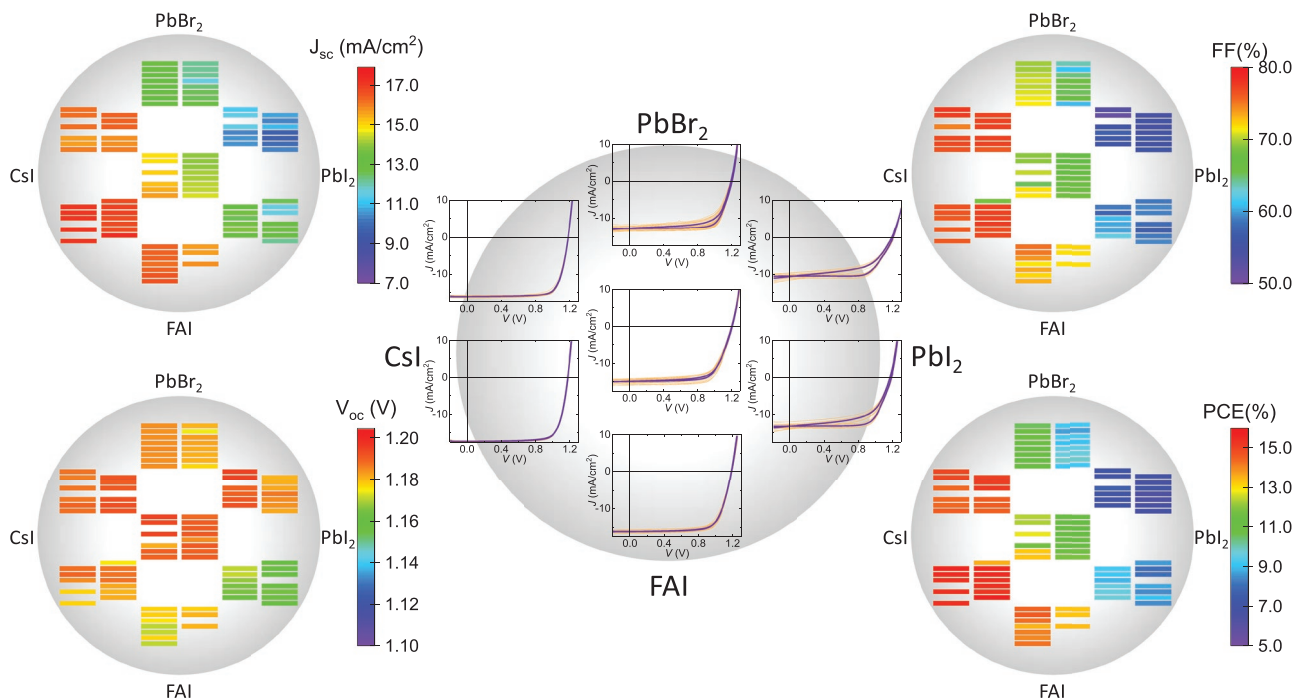www.advmatinterfaces.de

Figure 2. Results of combinatorial deposition of wide bandgap perovskite solar cells. 112 points color maps for J_{sc}, V_{oc}, (top) FF, and PCE (bottom) are shown together with the J–V curves for each substrate (the mathematical average of all J–V curves for each substrate are shown as a thick blue line). The deposition rates for PbI_2, $PbBr_2$, CsI, and FAI are those reported in Table 1 as the initial parameter set.

Samples on the right side of the sample holder, where PbI_2 is sublimed, show hindered charge extraction (FF roughly in the 50–60% range), as well as hysteresis in the J–V curves when measured in forward (short- to open-circuit) and reverse (open- to short-circuit) bias direction. J–V hysteresis is completely suppressed for substrates placed on top of the CsI and FAI thermal sources. The PCE map shows an obvious gradient going from the top right to the bottom left of the sample holder. The lowest values (6–9%) were found for pixels located in the vicinity of the PbI_2 and $PbBr_2$ sources, mainly due to the lower photocurrent and FF. The best-performing solar cells are located in the bottom-left part of the maps, with most of the pixels in the 14–15% PCE range.

In principle, we expect the average performance of solar cells on the central substrate to resemble that of devices deposited with the same set of deposition rates, but with a rotating sample holder. Hence, we slightly increased r(CsI) from 0.4 to 0.5 Å s^{-1} in a second combinatorial deposition, to modify the CCS of the perovskite and analyzed the spatial distribution of the corresponding solar cell's characteristics (**Figure 3**).

One can immediately notice how the gradients in the different color maps are altered upon increasing r(CsI). J_{sc} is larger in the central substrate, from 13–14 mA cm^{-2} to ≥16 mA cm^{-2}, while the highest values (up to 17 mA cm^{-2}) are still found for the three substrates placed on top of the CsI and FAI sources (bottom-left part of the map). In these very same substrates, however, the V_{oc} was found to diminish substantially (to 1.10–1.12 V), likely a consequence of the high Cs$^+$ content which can introduce nonradiative recombination channels in the material, as we have

previously observed for similar compositions.[41] The gradient of the FF was found to be reduced, with high and rather homogeneous FF (mostly in the 75–80% range) in most of the solar cells, excluding those prepared near the PbI_2 source, that shows hindered charge extraction and low FF as also observed in the previous combinatorial deposition. The resulting PCE map shows that the highest values have been shifted closer to the center of the substrate, as hypothesized above. The solar cells in the central substrate have PCE >14% on average, while there is more spreading in the pixels of the substrate standing between the CsI and FAI sources (bottom-left). In these substrates, some solar cells show higher (closer to 15%) PCE due to higher J_{sc}, while in other pixels the PCE is reduced due to a low V_{oc}, as previously discussed.

The J–V curves of the central and the bottom substrate show negligible hysteresis and almost no spreading in performance among the individual pixels. On the other substrates of this run, we observe that there is either a spreading in performance among individual pixels, and/or J–V hysteresis. In particular, closer to the PbX_2 source, a more significant spreading, and hysteresis is observed. Using the combinatorial approach, we see that a small change in the deposition rate of a single precursor generates a whole new set of samples with different compositions and solar cell parameters that can be investigated.

The CCS library obtained via combinatorial vacuum deposition of perovskites, as shown in Figure 3, has been subsequently characterized by spatially-resolved structural, morphological, and optical analysis. **Figure 4** shows the X-ray
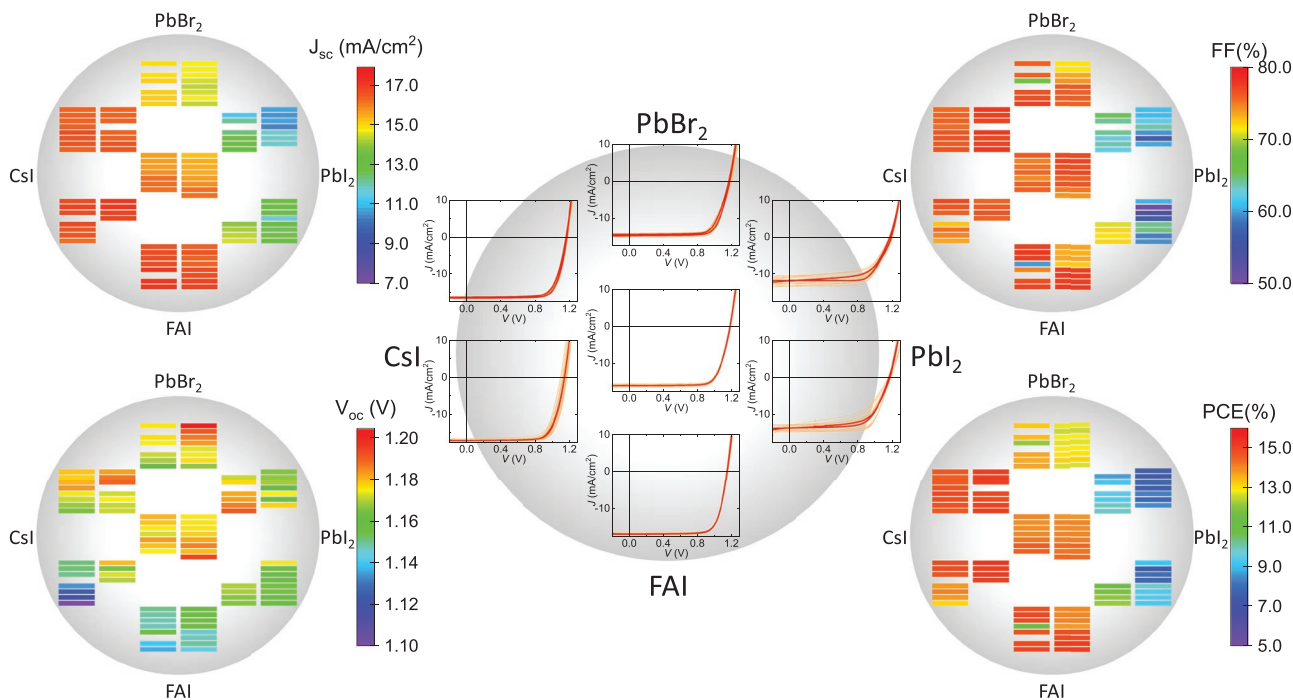
**ADVANCED
SCIENCE NEWS**
www.advancedsciencenews.com

**ADVANCED
MATERIALS
INTERFACES**
www.advmatinterfaces.de

Figure 3. Results of combinatorial deposition of wide bandgap perovskite solar cells. 112 points color maps for J_{sc}, V_{oc}, (top) FF, and PCE (bottom) are shown together with the J–V curves for each substrate (the mathematical average of all J–V curves for each substrate are shown as a thick red line). The deposition rates for PbI_2, $PbBr_2$, and FAI are the same as in Figure 2, while the r(CsI) is increased from (A) 0.4 Å s^{-1} to (B) 0.5 Å s^{-1}.

diffraction (XRD) and Scanning Electron Microscopy (SEM) characterization of different samples obtained without rotation. XRD is typically limited in spatial resolution, hence it was collected by measuring the 4 corners of each of the 7 substrates (28 measurements). Figure 4a highlights representative diffractograms for the 7 substrates focusing on the most relevant regions ($2\theta = 12°–15°$ and $2\theta = 27°–31°$ approximately; full diffractograms are given in Figures S1 (Supporting Information).

There are clear differences between the bottom-left part closer to the A-cation sources (CsI and FAI) and the top-right part closer to the B-cation sources (PbI_2 and $PbBr_2$), meaning that a gradient in crystallographic properties is established in this case. In particular, two facts can be easily observed qualitatively when moving from the bottom-left (A-rich) to the top-right (Pb-rich) direction: i) the main signal for crystalline PbI_2 ($2\theta = 12.7°$) relative to the perovskite peaks ($2\theta = 14.3°$ and $2\theta = 28.8°$, approximately) increases, and ii) the perovskite peaks become broader and split into multiple reflections. The latter observation can be related to PbX_6 octahedra rotation and tilting from the cubic perovskite crystal structure towards a lower-symmetry configuration, as further discussed in the following.[67]

In order to go beyond these qualitative observations, we performed a whole-pattern fit of all 28 diffractograms (4 corners of each of the 7 substrates) for a semi-quantitative analysis. Details of the fitting procedure can be found in the experimental section. Figure 4b represents the relative PbI_2/Perovskite signal, which is established as the ratio between the calculated

intensities of the (001) peak from PbI_2 (at $\approx 2\theta = 12.7°$) and the (020) peak of the perovskite phase ($\approx 2\theta = 14.3°$). These values are obviously related to the relative amounts of crystalline PbI_2 and perovskite in the film. However, due to the high crystallographic texture (preferential orientation) that is typical of vacuum-deposited thin films,[68] it is not possible to quantify this ratio. Nevertheless, the semi-quantitative analysis presented in Figure 4b clearly highlights the gradient in the PbI_2/perovskite ratio, with noticeably higher fractions towards the Pb sources, as could be expected. However, we note that the ratio may vary both because of an increase in crystalline PbI_2 and/or because of a decrease in crystalline perovskite (see further discussion on SEM characterization).

In addition, the shapes of the perovskite phase signals differ, as is clearly seen in the range $2\theta = 27°–31°$. It is well known that depending on the exact composition as well as other factors (e.g., temperature) lead halide perovskites can crystallize in a higher-symmetry cubic crystal structure or lower-symmetry tetragonal or orthorhombic structures.[69] Diffractograms will show more distinct peaks when the symmetry of the phase is reduced. To assess this, we fitted all diffractograms considering an orthorhombic perovskite phase (space group = Pnma; a = 8.1 Å, b = 12.4 Å, c = 8.3 Å). This allows more freedom in the whole-pattern Le Bail fit and can lead to good fits even in the case of a cubic phase (the cubic perovskite can be seen as a particular or limited case of the orthorhombic structure, while the opposite is not true). As a result, we are in fact considering three overlapping peaks $\approx 2\theta = 28.1°$, $2\theta = 28.4°$, and $2\theta = 28.8°$, corresponding to the (122), (221), and (040) planes, respectively.

ADVANCED
SCIENCE NEWS
www.advancedsciencenews.com

ADVANCED
MATERIALS
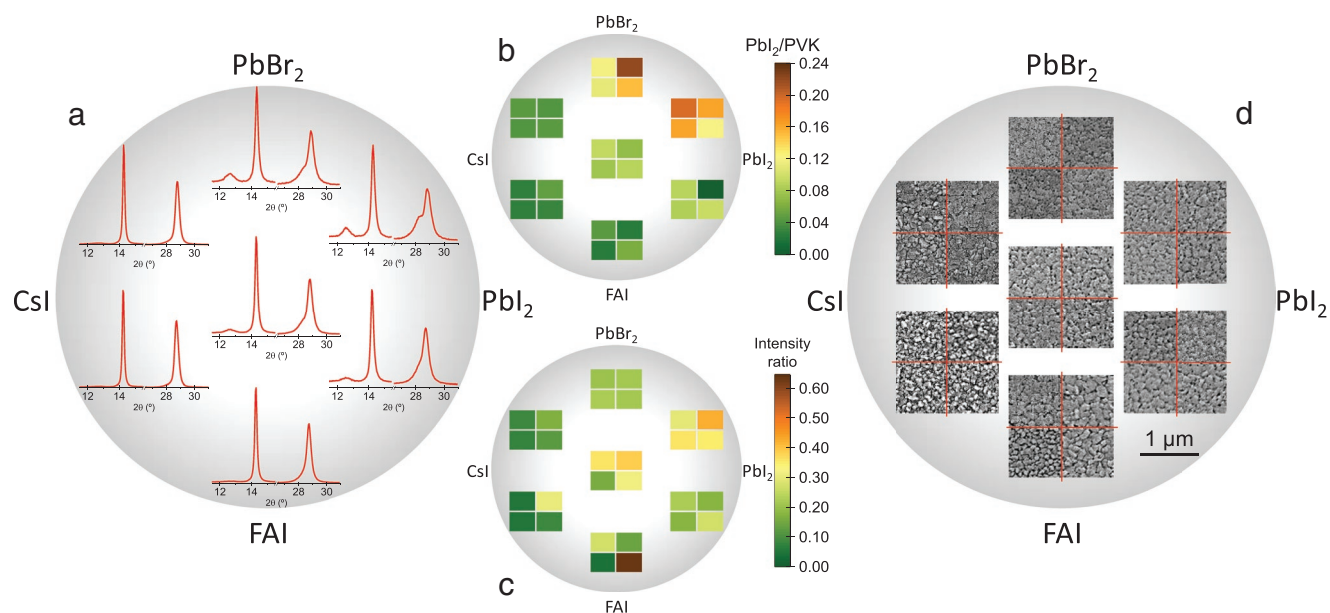**INTERFACES**
www.advmatinterfaces.de

Figure 4. Structural and morphological analysis of the material library. a) Selected XRD patterns for each of the 7 substrates, highlighting the most relevant regions ($2\theta = 12°–15°$ and $2\theta = 27°–31°$ approximately). b) Color map of the ratio between the calculated intensities of the (001) peak from PbI_2 ($\approx 2\theta = 12.7°$) and the (020) peak of the perovskite phase ($\approx 2\theta = 14.3°$). c) Color map of the intensity ratio between the sum of (122) and (221) peaks over the main (040) one, where lower values indicate predominance of the higher symmetry cubic phase over tetragonal and/or orthorhombic distortions. d) SEM images of selected areas of the surfaces of the seven substrates.

Figure 4c represents the intensity ratio between the sum of the (122) and (221) peaks over the main (040) one. In the case of a cubic perovskite, this ratio should be 0 as only one peak is present. Hence, green pixels represent pure, or higher fraction of a cubic perovskite, and orange/brown pixels represent a higher fraction of lower-symmetry orthorhombic (or tetragonal) perovskites. The Goldschmidt tolerance factor $t = (r_A + r_X)/\sqrt{2(r_B + r_X)}$ where r_A, r_B, and r_X are the ionic radiuses of the A cation, B cation, and halide, respectively, can be used to predict lead halide perovskite crystal structures. A low t value (low r_A and high r_B) $\approx 0.7–0.8$ will generally lead to orthorhombic perovskites, while a higher value of $t \approx 0.9–1.0$ will lead to cubic perovskites. Here, deriving a value for t is not straightforward given the multi-cation and multi-anion gradients formed in the combinatorial deposition. However, it is significant that, aside from one outlier pixel close to the FAI source, the values in Figure 4c are higher towards the Pb-sources (in particular closer to the PbI_2 source) and lower towards the A-cation sources. Indeed, this highlights an A-cation deficiency in the top-right part of the sample holder (closer to the PbX_2 sources) that leads not only to higher PbI_2 over perovskite ratios (Figure 4b) but also to lower-symmetry perovskites (Figure 4c).

SEM characterization (Figure 4d) also reveals a more defined morphology towards the A-sources and a seemingly more amorphous behavior towards the Pb-sources. This is in good agreement with the XRD characterization. As we previously mentioned, the higher PbI_2/perovskite ratio towards the B-sources (Figure 4b) may not only come from a higher amount of crystalline PbI_2 in the film but also from a lower amount of crystalline perovskite. When the diffractograms are overlapped without normalization (see Figure S2, Supporting Information), it is noticeable that the perovskite peaks are significantly more intense in samples that are closer to the A-cation sources (CsI and FAI). As all diffractograms are acquired with identical instrumental conditions, it is reasonable to ascribe the higher intensity to a higher fraction of crystalline (versus amorphous) perovskites in these samples. In summary, Figure 4 reveals a gradient in structural and morphological properties. Overall, a dominant perovskite phase is observed in all films with a minor contribution from PbI_2. In this sense, the crystallization is not highly inhomogeneous. Nevertheless, subtle differences generally point towards a deficiency of A-cations toward the PbX_2 sources, which leads to poorer morphology and crystallinity.

We then studied the optical properties of the material library, such as optical bandgap (E_g) and photoluminescence quantum yield (PLQY), and correlated them with elemental composition. **Figure 5**a shows the E_g map extracted from the onset of the optical absorption of the films, measured at 112 points in the exact same position as the solar cells described in Figure 3 (selected absorption and PL spectra for each substrate are shown in Figure 5c). A clear E_g gradient can be observed in the map, with lower values (1.7 eV) close to the FAI source, increasing towards the center of the sample holder (1.73–1.74 eV), and maximum E_g values ≥ 1.76 eV in the films deposited near the $PbBr_2$ source, on the top of the map. This small variation across the holder would have been ignored unless high throughput measurements were performed to give high-resolution maps, showing a clear bandgap trend moving from the A-cation sources to the PbX_2 sources.

While E_g seems strongly related with the bromide content in the perovskite (as seen from the vertical gradient of the map in Figure 5a), a slight but apparent horizontal gradient can also be observed: in the bottom part of the sample holder, the
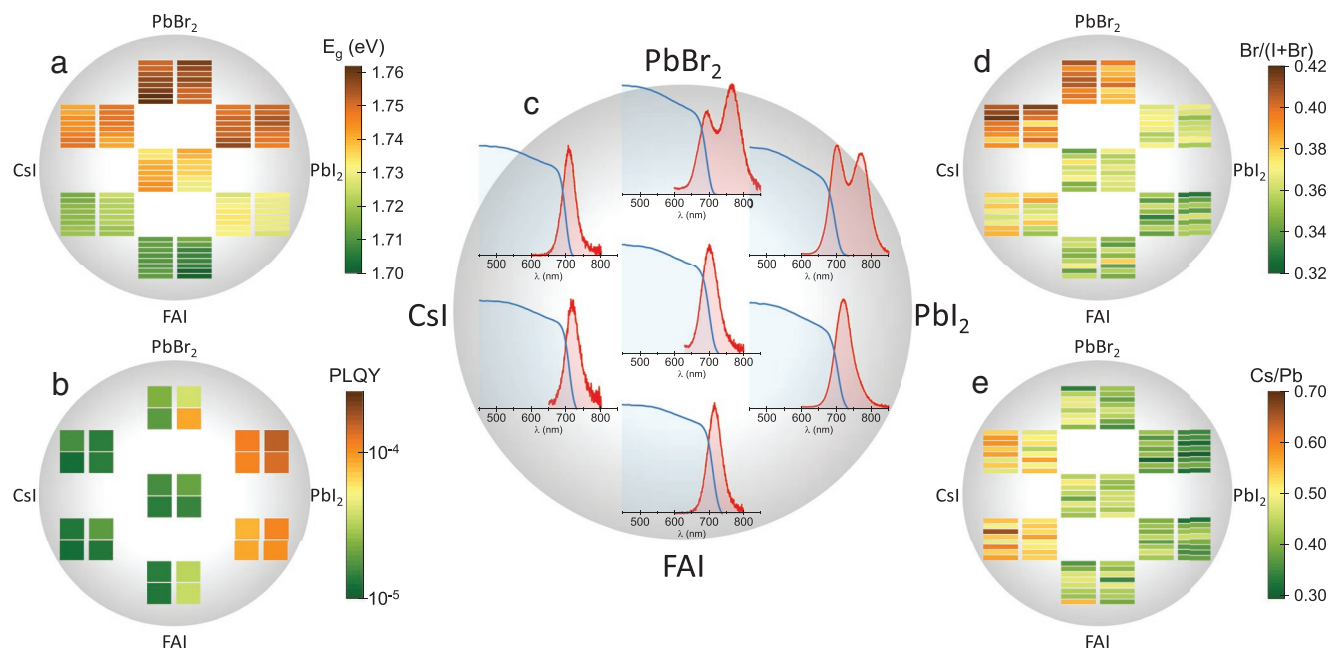
Figure 5. Optical and elemental characterization of the library of materials. a) Bandgap (E_g) color map extracted from spatially resolved optical absorption. b) PLQY map, measured at the corners of each substrate. c) Representative absorption (blue) and PL (red) spectra for each substrate. EDS color map of d) Br/(Br + I) and e) Cs/Pb concentration ratios.

materials grown closer to the PbI_2 source (right) have larger E_g (≥1.73 eV) as compared to those near the CsI source (left, 1.71–1.72 eV). This might appear counterintuitive, however, partially converted perovskites (with residual PbX_2 phase) have been reported to show a wider bandgap as compared to the same phase-pure perovskite.[70] Here, the perovskite films in the vicinity of the PbI_2 source have a lower crystallinity and higher PbI_2/perovskite intensity ratio, as observed by XRD (Figure 4a,b). This implies a lower degree of conversion of the precursors into perovskite, hence a wider E_g.

We have also measured the elemental composition of the materials library by energy-dispersive X-ray spectroscopy (EDS) in an SEM, for the same position where the E_g was estimated. Figure 5d shows a map of bromide ratio, expressed as the bromide concentration normalized for the sum of iodide and bromide content, while Figure 5e shows the Cs/Pb ratio map. Cs and Br were chosen because only one source is depositing these elements, allowing the effect of deposition without rotation and source location to be evaluated readily. The Cs content decreases gradually from perovskites grown closest to the CsI source, to those farthest away and close to the PbI_2 substrate, leading to a clear horizontal gradient in the EDS map (Figure 5e). The gradient in the bromide mapping (Figure 5d) is not completely aligned with the E_g gradient (Figure 5a), suggesting a preferential bromide adsorption in Cs-rich formulations, and a lower intake for Pb-rich materials. Also, the bromide differential concentration over the whole material library is small (10% variation), while the Cs concentration decreases from 70% (near CsI) to 30% (far from CsI). These observations indicate a different evaporation cone for the two materials: that of CsI is more directional, with most of the Cs being incorporated in the films directly on top of the CsI

thermal source, while that of $PbBr_2$ distributes more homogeneously over the whole substrate holder.

Calibrated, absolute PL measurements were also carried out on the 4 corners of each of the 7 substrates, allowing to map the PLQY over the material library. The PLQY map (Figure 5b) shows a clear trend, with Cs-rich compositions showing the lowest values (≈10⁻⁵), and rising luminescence efficiency for materials on the right side of the sample holders, more rich in PbI_2. In all cases, however, the PLQY is low (maximum ≈3 × 10⁻⁴), indicating the presence of non-radiative recombination channels in the perovskite bulk or at its surface.[71–73] An important observation needs to be made regarding the PL spectra and the corresponding PLQY: the PLQY is calculated from the integrated intensity of the whole PL spectrum, and hence it contains all contributions arising from impurities or phase segregation. Considering the PL spectra reported in Figure 5c for each substrate, we can indeed observe that the PL spectra show two components for samples in the top-right part of the sample holder. This is a signature of the perovskite demixing into bromide-rich and iodide-rich domains commonly referred to as halide segregation.[34,32,33] This effect is photoinduced and dynamic, and is only observed here for perovskite formulations which are lead bromide-rich and Cs-poor (see Figure S3, Supporting Information), in agreement with previous reports.[74] As a matter of fact, the sample with the higher bromide content (top-left in Figure 5d) does not show any detectable halide segregation (Figure 5c), because of its equally high Cs concentration (Figure 5e). From the PLQY map, the quasi-Fermi level splitting (QFLS) was estimated using the reciprocity relation.[75] The QFLS map (see Figure S4, Supporting Information, where it is compared with the corresponding measured V_{oc}) shows a clear trend, increasing from

1.15 eV (bottom-left) to 1.25–1.30 eV in the top-right part of the material library. The QFLS gradient is a combination of the vertical gradient in bandgap and the horizontal gradient in PLQY. This trend agrees with the V_{oc} observed in the devices, the lowest values being those of solar cells prepared between the CsI and FAI sources. The outliers in the top-right substrate of the QFLS map (highest QFLS values approaching 1.3 eV in Figure S4, Supporting Information) are consequence of the PL peak splitting described above, which makes the QFLS calculation incorrect and is detrimental to the V_{oc} of the solar cells.

To briefly summarize, using CMS together with vacuum deposition we were able to deposit a CCS library, where the gradients are directly controllable by the deposition rate of each precursor. This approach shows great potential for the development of novel perovskite formulations by multi-source vacuum deposition. We observed, in a single combinatorial deposition run, several features of the $FA_{1-n}Cs_nPb(I_{1-x}Br_x)_3$ perovskite family, which otherwise would have taken several batches to be identified. Among these, Cs-rich wide bandgap formulations are found to be more crystalline and with a more defined morphology, resulting in high J_{sc} and FF. However, the same Cs-rich perovskites have lower PLQY, leading to a higher V_{oc} loss in solar cells. While Cs-rich formulations have a high symmetry crystal structure (cubic), Cs-poor and Pb-rich perovskites are more disordered, with lower symmetry tetragonal or orthorhombic phases. Pb-rich perovskites with unconverted PbI_2 precursors show a wider bandgap as compared to phase-pure perovskites. Also, as expected, halide segregation is observed only when high concentration of bromide is not compensated by sufficient Cs in the perovskite structure.

The combinatorial deposition can also be directly applied to the development of optoelectronic devices. As we showed in Figure 3, tuning the deposition rates shift the gradients accordingly. To explore the potential of this method, we performed another deposition run, using the same parameter set used in Figure 3, but this time with sample rotation. In a first approximation, the central substrate sees similar deposition rates for the different precursors in a deposition with and without rotation. The performance of the corresponding perovskite solar cells is reported and compared with that of devices obtained without rotation (central substrate in Figure 3). **Figure 6**a shows the J–V curves under illumination for the central substrate obtained without rotation, and Figure 6b those for the solar cells obtained with rotation. In the latter, we show the J–V curves for two substrates, one in the center of the sample holder, and the other on the edge (to check for the homogeneity induced by the sample rotation). The PL spectra of the perovskites obtained with each method are reported as an inset, and fitted with a Voigt function to extract the peak center. A summary of the PV parameters for both batches of devices is reported in Figure 6c. The material properties appear to be similar, as the center of the PL spectra of the two batches is exactly at the same wavelength (only a small deviation in the peak width can be observed). Solar cells prepared with the two methods behave similarly in absolute values, especially when looking at V_{oc}, FF, and resulting PCE. The main difference can be seen in the spread of the J_{sc}, which

is larger for the solar cells prepared without rotation. This was already seen in Figure 3 and is expected in view of the bandgap variation induced by the gradient in chemical composition, also reported in Figure 5a. The similarity of the two samples teaches us that the middle sample on the holder can be compared to a rotating sample. By placing more samples on the fixed holder, we can exploit the deposition to study more compositions, accelerating the progress of vacuum-deposited halide perovskite research.

3. Conclusions

We applied CMS to vacuum deposition process to the screening of lead halide perovskite formulations starting from 4 precursors placed in different thermal sources. By fixing the sample holder and spatially analyzing the performance of the solar cells and the material properties, we are able to extract a large amount of information and screen a wide parameter space in a single deposition run. As a model system, we targeted the wide bandgap perovskite of the type $FA_{1-n}Cs_nPb(I_{1-x}Br_x)_3$, which can be vacuum-processed starting from FAI, CsI, PbI_2, and $PbBr_2$. Several properties of this family of materials have been identified in a single combinatorial deposition run, in contrast to standard vacuum deposition experiments with rotating sample holders where only one set of parameters can be studied for each batch. CCS can be fine-tuned by adjusting the deposition parameters, and solar cells obtained in the central substrate (with equal distance from the 4 thermal sources) resemble closely those obtained with the same deposition parameters but with sample rotation, which is routinely used for the fabrication of perovskite solar cells. This feature can speed up substantially the development of novel perovskite composition: high throughput experiments can be carried out with a fixed substrate holder, the deposition rates can be adjusted by shifting the desired materials parameters towards the center of the sample holder, and finally this set of parameters can be used in a standard deposition process with sample rotation. We envision this route as the direction to take for the future development of vacuum-processed multi-component optoelectronic devices.

4. Experimental Section

Materials: N4,N4,N4′,N4′-tetra([1,1′-biphenyl]-4-yl)-[1,1′:4′,1′-terphenyl]-4,4′-diamine (TaTm) was provided by Novaled GmbH and fullerene (C60) was purchased from Merck KGaA. PbI_2, MoO_3, and bathocuproine (BCP) were purchased from Luminescence Technology Corp. $CHNH_2NH_2I$ (FAI) was purchased from Greatcell Solar. $PbBr_2$ was obtained from Tokyo Chemical Industry. All materials were used as received.

Vacuum Deposition of Perovskite Films and Solar Cells: ITO-coated glass substrates were subsequently cleaned with soap, water, and isopropanol in an ultrasonic bath, followed by 20 min UV-ozone treatment. The substrates were transferred to a vacuum chamber integrated in a nitrogen-filled glovebox and evacuated to a pressure of 10^{-6} mbar for the charge extraction layers' deposition. In general, the deposition rate for the TaTm and C60 was 0.5 Å s^{-1} while the thinner BCP layer was sublimed at 0.2 Å s^{-1}. MoO_3 and Ag were deposited in a second vacuum chamber using aluminum boats as sources, by applying currents ranging from 2.0 to 4.5 A. The perovskite was evaporated in another vacuum chamber, equipped with four evaporation sources (Creaphys
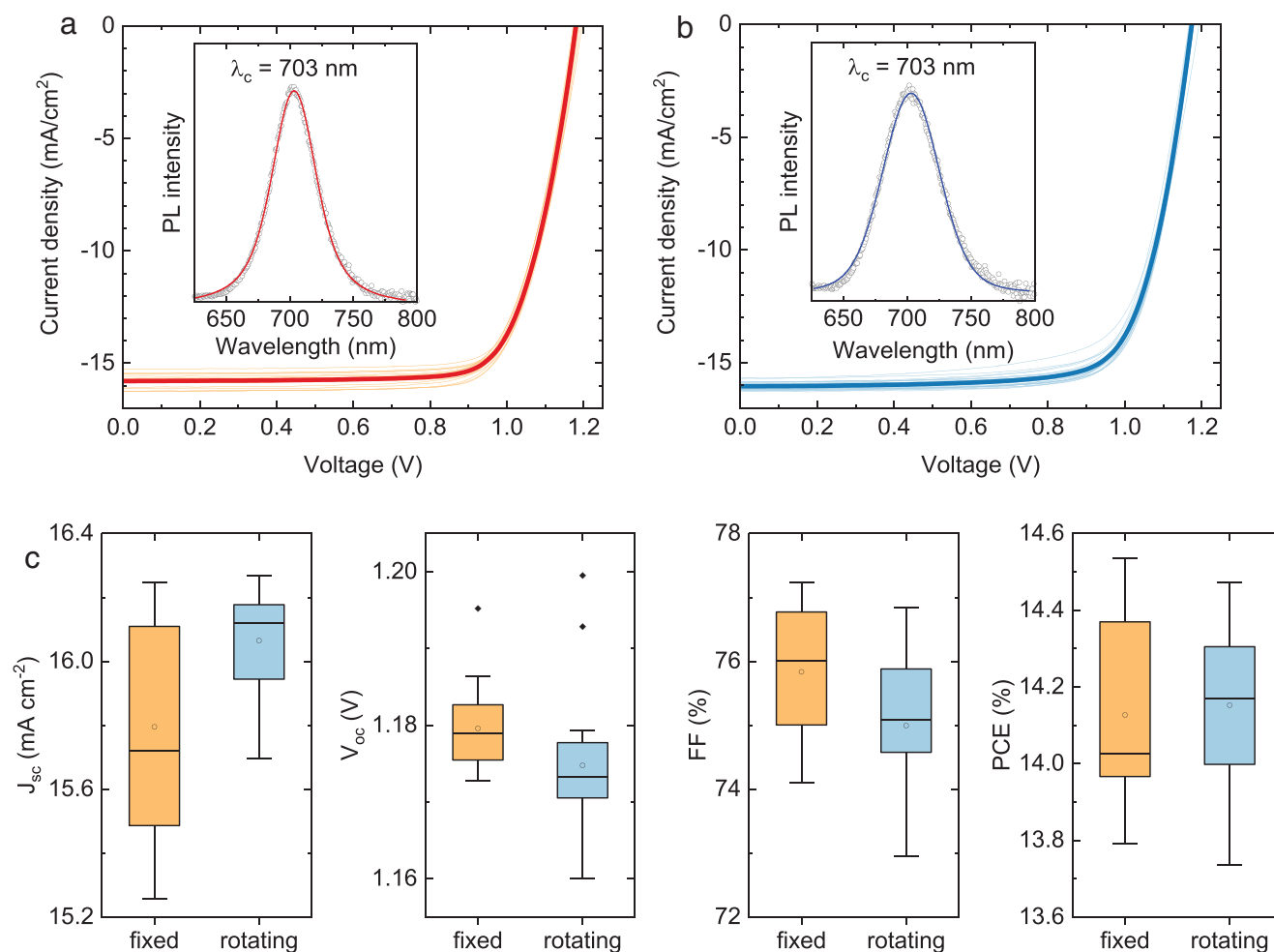
Figure 6. Comparison of solar cells obtained with fixed and rotating sample holders. a) J–V curves under illumination for solar cells in the center of a non-rotating (fixed) sample holder and b) J–V curves under illumination for solar cells obtained in a controlled deposition with sample rotation (the J–V curves for two substrates, one on the center and one on the edge of the sample holder are reported). Light colors indicate J–V curves for each single pixel, while the thick lines are the mathematical average of all J–V curves. The inset in (a) and (b) show the PL spectra fitted with a Voigt function to quantify the peak center. c) Distribution of the PV parameters for the two sets of solar cells, obtained without and with sample rotation. The same deposition rates are used: $r(PbI_2) = 1.0$ Å s^{-1}; $r(PbBr_2) = 0.2$ Å s^{-1}; $r(FAI) = 0.8$ Å s^{-1}; $r(CsI) = 0.5$ Å s^{-1}.

and with independent temperature controllers and shutters. All sources had a dedicated QCM sensor above, and an additional one was installed close to the substrates for the overall deposition rate measurement. All sources were individually calibrated for their respective materials and no cross-reading between different materials was ensured by the position of the sources, shutters, and sensors. Details of the geometry and deposition rates were provided in the main text. During the perovskite deposition, the pressure of the chamber was maintained at 8×10^{-6} mbar and the substrates were kept at room temperature. Typical sublimation temperatures for the precursors were 150 °C for FAI, 310 °C for PbI$_2$, 280–300 °C for PbBr$_2$, and 490–520 °C for CsI.

Material and Device Characterization: The J–V curves for the solar cells were recorded using a Keithley 2612A SourceMeter in a −0.2 and 1.3 V voltage range, with 0.01 V steps and integrating the signal for 20 ms after a 10 ms delay, corresponding to a scan speed of ≈0.3 V s^{-1}. The custom-made sample holder and electronics allow to measure all 16 pixels on each device automatically. The devices were illuminated under a Wavelabs Sinus 70 LED solar simulator. The light intensity was calibrated before every measurement using a calibrated Si reference diode. The crystalline structure of the powder and film samples was studied by X-ray diffraction (XRD). The patterns were collected in Bragg-Brentano

geometry on an Empyrean PANalytical powder diffractometer with a copper anode operated at 45 kV and 40 mA. Further analysis including Le Bail fits was performed with Fullprof software. SEM top-view images were taken using the HRSEM (FEI, Magellan 400 L) at 4 kV and 0.4 nA. The seven samples of FA$_{1-n}$Cs$_n$Pb(I$_{1-x}$Br$_x$)$_3$ compositional spread were deposited on glass and were measured using energy-dispersive X-ray spectroscopy (EDS). The EDS spectra were obtained by an 80 mm^2 X-max detector (Oxford Instruments) coupled to the HRSEM at 30 kV. On each substrate, 16 points corresponding to the positions in Figure 1 were measured and then analyzed using the Aztec software (Oxford Instruments). The photoluminescence spectra were measured with an Avantes Avaspec2048 spectrometer and films were illuminated with a diode laser of integrated optics, emitting at 522 nm. All the spectra were collected with an integration time of 1 s. Scanning optical spectroscopy measurements were performed on 16 points (corresponding to the positions in Figure 1). Optical absorption measurements were performed using total transmission (TT) and total reflection (TR) over 400–1000 nm spectral range in N$_2$ atmosphere. The system was optical fiber-based and consisted of a CCD array spectrometer (USB4000, Ocean Optics) and two integrating spheres.[76] The measurement points were circular with a diameter of 3 mm. The absorptance was calculated based on the

total transmission and total reflection measurements as $A = 100-TT-TR$. Optical bandgaps were calculated from the absorption onset.

Supporting Information

Supporting Information is available from the Wiley Online Library or from the author.

Acknowledgements

Conflict of Interest

The authors declare no conflict of interest.

Data Availability Statement

The data that support the findings of this study are available from the corresponding author upon reasonable request.

Keywords

[1] P. K. Nayak, S. Mahesh, H. J. Snaith, D. Cahen, *Nat. Rev. Mater.* **2019**, *4*, 269.

[2] H. Min, D. Y. Lee, J. Kim, G. Kim, K. S. Lee, J. Kim, M. J. Paik, Y. K. Kim, K. S. Kim, M. G. Kim, T. J. Shin, S. Il Seok, *Nature* **2021**, *598*, 444.

[3] S. De Wolf, J. Holovsky, S.-J. Moon, P. Löper, B. Niesen, M. Ledinsky, F.-J. Haug, J.-H. Yum, C. Ballif, *J. Phys. Chem. Lett.* **2014**, *5*, 1035.

[4] S. D. Stranks, G. E. Eperon, G. Grancini, C. Menelaou, M. J. P. Alcocer, T. Leijtens, L. M. Herz, A. Petrozza, H. J. Snaith, *Science* **2013**, *342*, 341.

[5] Q. Dong, Y. Fang, Y. Shao, P. Mulligan, J. Qiu, L. Cao, J. Huang, *Science (80-.).* **2015**, *347*, 967.

[6] J. M. Frost, K. T. Butler, F. Brivio, C. H. Hendon, M. van Schilfgaarde, A. Walsh, *Nano Lett.* **2014**, *14*, 2584.

[7] W.-J. Yin, T. Shi, Y. Yan, *Adv. Mater.* **2014**, *26*, 4653.

[8] J. M. Azpiroz, E. Mosconi, J. Bisquert, F. De Angelis, *Energy Environ. Sci.* **2015**, *8*, 2118.

[9] A. Buin, R. Comin, J. Xu, A. H. Ip, E. H. Sargent, *Chem. Mater.* **2015**, *27*, 4405.

[10] Z. Li, T. R. Klein, D. H. Kim, M. Yang, J. J. Berry, M. F. A. M. van Hest, K. Zhu, *Nat. Rev. Mater.* **2018**, *3*, 18017.

[11] M. Liu, M. B. Johnston, H. J. Snaith, *Nature* **2013**, *501*, 395.

[12] J. Ávila, C. Momblona, P. P. Boix, M. Sessolo, H. J. Bolink, *Joule* **2017**, *1*, 431.

[13] Q. Guesnay, F. Sahli, C. Ballif, Q. Jeangros, *APL Mater.* **2021**, *9*, 100703.

[14] Y. Jiang, S. He, L. Qiu, Y. Zhao, Y. Qi, *Appl. Phys. Rev.* **2022**, *9*, 021305.

[15] S.-R. Bae, D. Y. Heo, S. Y. Kim, *Mater. Today Adv.* **2022**, *14*, 100232.

[16] V. S. Chirvony, K. S. Sekerbayev, D. Pérez-del-Rey, J. P. Martínez-Pastor, F. Palazon, P. P. Boix, T. I. Taurbayev, M. Sessolo, H. J. Bolink, *J. Phys. Chem. Lett.* **2019**, *10*, 5167.

[17] J. B. Patel, A. D. Wright, K. B. Lohmann, K. Peng, C. Q. Xia, J. M. Ball, N. K. Noel, T. W. Crothers, J. Wong-Leung, H. J. Snaith, L. M. Herz, M. B. Johnston, *Adv. Energy Mater.* **2020**, *10*, 1903653.

[18] J. Li, H. Wang, X. Y. Chin, H. A. Dewi, K. Vergeer, T. W. Goh, J. W. M. Lim, J. H. Lew, K. P. Loh, C. Soci, T. C. Sum, H. J. Bolink, N. Mathews, S. Mhaisalkar, A. Bruno, *Joule* **2020**, *4*, 1035.

[19] M. R. Filip, G. E. Eperon, H. J. Snaith, F. Giustino, *Nat. Commun.* **2014**, *5*, 5757.

[20] R. Prasanna, A. Gold-Parker, T. Leijtens, B. Conings, A. Babayigit, H.-G. Boyen, M. F. Toney, M. D. McGehee, *J. Am. Chem. Soc.* **2017**, *139*, 11117.

[21] F. Ünlü, E. Jung, J. Haddad, A. Kulkarni, S. Öz, H. Choi, T. Fischer, S. Chakraborty, T. Kirchartz, S. Mathur, *APL Mater.* **2020**, *8*, 070901.

[22] S. Chatterjee, A. J. Pal, *J. Mater. Chem. A* **2018**, *6*, 3793.

[23] A. Kama, S. Tirosh, A. Itzhak, M. Ejgenberg, D. Cahen, *ACS Appl. Energy Mater.* **2022**, *5*, 3638.

[24] J. H. Noh, S. H. Im, J. H. Heo, T. N. Mandal, S. Il Seok, *Nano Lett.* **2013**, *13*, 1764.

[25] L. Protesescu, S. Yakunin, M. I. Bodnarchuk, F. Krieg, R. Caputo, C. H. Hendon, R. X. Yang, A. Walsh, M. V. Kovalenko, *Nano Lett.* **2015**, *15*, 3692.

[26] J. Borchert, R. L. Milot, J. B. Patel, C. L. Davies, A. D. Wright, L. Martínez Maestro, H. J. Snaith, L. M. Herz, M. B. Johnston, *ACS Energy Lett.* **2017**, *2*, 2799.

[27] L. Gil-Escrig, C. Dreessen, I. C. Kaya, B.-S. Kim, F. Palazon, M. Sessolo, H. J. Bolink, *ACS Energy Lett.* **2020**, *5*, 3053.

[28] K. B. Lohmann, S. G. Motti, R. D. J. Oliver, A. J. Ramadan, H. C. Sansom, Q. Yuan, K. A. Elmestekawy, J. B. Patel, J. M. Ball, L. M. Herz, H. J. Snaith, M. B. Johnston, *ACS Energy Lett.* **2022**, *7*, 1903.

[29] M. Roß, S. Severin, M. B. Stutz, P. Wagner, H. Köbler, M. Favin-Lévêque, A. Al-Ashouri, P. Korb, P. Tockhorn, A. Abate, B. Stannowski, B. Rech, S. Albrecht, *Adv. Energy Mater.* **2021**, *11*, 2101460.

[30] G. Longo, C. Momblona, M.-G. La-Placa, L. Gil-Escrig, M. Sessolo, H. J. Bolink, *ACS Energy Lett.* **2018**, *3*, 214.

[31] J. Huang, S. Xiang, J. Yu, C.-Z. Li, *Energy Environ. Sci.* **2019**, *12*, 929.

[32] E. T. Hoke, D. J. Slotcavage, E. R. Dohner, A. R. Bowring, H. I. Karunadasa, M. D. McGehee, *Chem. Sci.* **2015**, *6*, 613.

[33] D. J. Slotcavage, H. I. Karunadasa, M. D. McGehee, *ACS Energy Lett.* **2016**, *1*, 1199.

[34] A. J. Knight, L. M. Herz, *Energy Environ. Sci.* **2020**, *13*, 2024.

[35] D. P. McMeekin, G. Sadoughi, W. Rehman, G. E. Eperon, M. Saliba, M. T. Horantner, A. Haghighirad, N. Sakai, L. Korte, B. Rech, M. B. Johnston, L. M. Herz, H. J. Snaith, *Science* **2016**, *351*, 151.

[36] K. A. Bush, K. Frohna, R. Prasanna, R. E. Beal, T. Leijtens, S. A. Swifter, M. D. McGehee, *ACS Energy Lett.* **2018**, *3*, 428.

[37] R. Ji, Z. Zhang, C. Cho, Q. An, F. Paulus, M. Kroll, M. Löffler, F. Nehm, B. Rellinghaus, K. Leo, Y. Vaynzof, *J. Mater. Chem. C* **2020**, *8*, 7725.

[38] Y. Chiang, M. Anaya, S. D. Stranks, *ACS Energy Lett.* **2020**, *5*, 2498.

[39] L. Gil-Escrig, C. Dreessen, F. Palazon, Z. Hawash, E. Moons, S. Albrecht, M. Sessolo, H. J. Bolink, *ACS Energy Lett.* **2021**, *6*, 827.

[40] K. B. Lohmann, S. G. Motti, R. D. J. Oliver, A. J. Ramadan, H. C. Sansom, Q. Yuan, K. A. Elmestekawy, J. B. Patel, J. M. Ball, L. M. Herz, H. J. Snaith, M. B. Johnston, *ACS Energy Lett.* **2022**, *7*, 1903.

[41] L. Gil-Escrig, C. Momblona, M.-G. La-Placa, P. P. Boix, M. Sessolo, H. J. Bolink, *Adv. Energy Mater.* **2018**, *8*, 1703506.

[42] I. Susic, L. Gil-Escrig, F. Palazon, M. Sessolo, H. J. Bolink, *ACS Energy Lett.* **2022**, *7*, 1355.

[43] A. M. Igual-Muñoz, J. Navarro-Alapont, C. Dreessen, F. Palazon, M. Sessolo, H. J. Bolink, *Chem. Mater.* **2020**, *32*, 8641.

[44] J. M. Ball, L. Buizza, H. C. Sansom, M. D. Farrar, M. T. Klug, J. Borchert, J. Patel, L. M. Herz, M. B. Johnston, H. J. Snaith, *ACS Energy Lett.* **2019**, *4*, 2748.

[45] M. Saliba, *Adv. Energy Mater.* **2019**, *9*, 1803754.

[46] X.-D. Xiang, *Annu. Rev. Mater. Sci.* **1999**, *29*, 149.

[47] L. Gouda, K. J. Rietwyk, J. Hu, A. Kama, A. Ginsburg, M. Priel, D. A. Keller, S. Tirosh, S. Meir, R. Gottesman, A. Zaban, *ACS Energy Lett.* **2017**, *2*, 2356.

[48] H.-N. Barad, M. Alarcón-Correa, G. Salinas, E. Oren, F. Peter, A. Kuhn, P. Fischer, *Mater. Today* **2021**, *50*, 89.

[49] P. J. McGinn, *ACS Comb. Sci.* **2019**, *21*, 501.

[50] I. Takeuchi, R. B. van Dover, H. Koinuma, *MRS Bull.* **2002**, *27*, 301.

[51] R. Potyrailo, K. Rajan, K. Stoewe, I. Takeuchi, B. Chisholm, H. Lam, *ACS Comb. Sci.* **2011**, *13*, 579.

[52] H. Näsström, P. Becker, J. A. Márquez, O. Shargaieva, R. Mainz, E. Unger, T. Unold, *J. Mater. Chem. A* **2020**, *8*, 22626.

[53] S. Moradi, S. Kundu, M. Rezazadeh, V. Yeddu, O. Voznyy, M. I. Saidaminov, *Commun. Mater.* **2022**, *3*, 13.

[54] X. Cao, L. Zhi, Y. Jia, Y. Li, K. Zhao, X. Cui, L. Ci, D. Zhuang, J. Wei, *ACS Appl. Mater. Interfaces* **2019**, *11*, 7639.

[55] M. Lv, X. Dong, X. Fang, B. Lin, S. Zhang, J. Ding, N. Yuan, *RSC Adv.* **2015**, *5*, 20521.

[56] I. Lignos, S. Stavrakis, G. Nedelcu, L. Protesescu, A. J. DeMello, M. V. Kovalenko, *Nano Lett.* **2016**, *16*, 1869.

[57] H. Anwar, A. Johnston, S. Mahesh, K. Singh, Z. Wang, D. A. Kuntz, I. Tamblyn, O. Voznyy, G. G. Privé, E. H. Sargent, *ACS Cent. Sci.* **2022**, *8*, 571.

[58] Y. Zhao, J. Zhang, Z. Xu, S. Sun, S. Langner, N. T. P. Hartono, T. Heumueller, Y. Hou, J. Elia, N. Li, G. J. Matt, X. Du, W. Meng, A. Osvet, K. Zhang, T. Stubhan, Y. Feng, J. Hauch, E. H. Sargent, T. Buonassisi, C. J. Brabec, *Nat. Commun.* **2021**, *12*, 2191.

[59] Y. Zhao, T. Heumueller, J. Zhang, J. Luo, O. Kasian, S. Langner, C. Kupfer, B. Liu, Y. Zhong, J. Elia, A. Osvet, J. Wu, C. Liu, Z. Wan, C. Jia, N. Li, J. Hauch, C. J. Brabec, *Nat. Energy* **2022**, *7*, 144.

[60] K. Kawashima, Y. Okamoto, O. Annayev, N. Toyokura, R. Takahashi, M. Lippmaa, K. Itaka, Y. Suzuki, N. Matsuki, H. Koinuma, *Sci. Technol. Adv. Mater.* **2017**, *18*, 307.

[61] P. Becker, J. A. Márquez, J. Just, A. Al-Ashouri, C. Hages, H. Hempel, M. Jošt, S. Albrecht, R. Frahm, T. Unold, *Adv. Energy Mater.* **2019**, *9*, 1900555.

[62] Q. Huang, F. Li, M. Wang, Y. Xiang, L. Ding, M. Liu, *Sci. Bull.* **2021**, *66*, 757.

[63] J. Li, P. Du, S. Li, J. Liu, M. Zhu, Z. Tan, M. Hu, J. Luo, D. Guo, L. Ma, Z. Nie, Y. Ma, L. Gao, G. Niu, J. Tang, *Adv. Funct. Mater.* **2019**, *29*, 1903607.

[64] S. Tao, I. Schmidt, G. Brocks, J. Jiang, I. Tranca, K. Meerholz, S. Olthof, *Nat. Commun.* **2019**, *10*, 2560.

[65] I. Levine, O. G. Vera, M. Kulbak, D.-R. Ceratti, C. Rehermann, J. A. Márquez, S. Levcenko, T. Unold, G. Hodes, I. Balberg, D. Cahen, T. Dittrich, *ACS Energy Lett.* **2019**, *4*, 1150.

[66] I. Levine, K. Shimizu, A. Lomuscio, M. Kulbak, C. Rehermann, A. Zohar, M. Abdi-Jalebi, B. Zhao, S. Siebentritt, F. Zu, N. Koch, A. Kahn, G. Hodes, R. H. Friend, H. Ishii, D. Cahen, *J. Phys. Chem. C* **2021**, *125*, 5217.

[67] Q. A. Akkerman, L. Manna, *ACS Energy Lett.* **2020**, *5*, 604.

[68] F. Palazon, D. Pérez-del-Rey, B. Dänekamp, C. Dreessen, M. Sessolo, P. P. Boix, H. J. Bolink, *Adv. Mater.* **2019**, *31*, 1902692.

[69] M. T. Weller, O. J. Weber, P. F. Henry, A. M. Di Pumpo, T. C. Hansen, *Chem. Commun.* **2015**, *51*, 4180.

[70] D. H. Cao, C. C. Stoumpos, C. D. Malliakas, M. J. Katz, O. K. Farha, J. T. Hupp, M. G. Kanatzidis, *APL Mater.* **2014**, *2*, 091101.

[71] S. Mahesh, J. M. Ball, R. D. J. Oliver, D. P. McMeekin, P. K. Nayak, M. B. Johnston, H. J. Snaith, *Energy Environ. Sci.* **2020**, *13*, 258.

[72] D. W. deQuilettes, K. Frohna, D. Emin, T. Kirchartz, V. Bulovic, D. S. Ginger, S. D. Stranks, *Chem. Rev.* **2019**, *119*, 11007.

[73] C. M. Wolff, P. Caprioglio, M. Stolterfoht, D. Neher, *Adv. Mater.* **2019**, *31*, 1902762.

[74] D. P. McMeekin, G. Sadoughi, W. Rehman, G. E. Eperon, M. Saliba, M. T. Hörantner, A. Haghighirad, N. Sakai, L. Korte, B. Rech, M. B. Johnston, L. M. Herz, H. J. Snaith, *Science* **2016**, *351*, 151.

[75] U. Rau, *Phys. Rev. B* **2007**, *76*, 085303.

[76] A. Y. Anderson, Y. Bouhadana, H.-N. Barad, B. Kupfer, E. Rosh-Hodesh, H. Aviv, Y. R. Tischler, S. Rühle, A. Zaban, *ACS Comb. Sci.* **2014**, *16*, 53.